Electrical Impedance Tomography: Modern advances and challenges

Jennifer Mueller

Department of Mathematics
and School of Biomedical Engineering
Colorado State University

Modern Challenges in Imaging in the Footsteps of Allan Cormack

Outline

Collaborations and support

Electrical Impedance Tomography

Low frequency, low amplitude current is applied on electrodes.

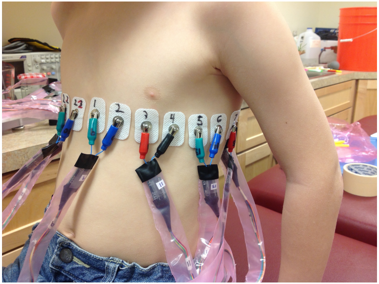

The voltage is measured and the conductivity and permittivity distributions inside are computed with mathematical algorithms.

The inverse problem is to determine these distributions from the voltage measurements on the electrodes.

The plotted conductivity and permittivity distributions results in images.

Medical Applications of EIT

EIT has a potentially important niche to fill:

- High temporal resolution: 50 frames/s is acheivable
- Continuous/ as needed patient monitoring
- Situations where CT and MRI are inaccessible

Medical Applications of EIT

EIT has a potentially important niche to fill:

- High temporal resolution: 50 frames/s is acheivable
- Continuous/ as needed patient monitoring
- Situations where CT and MRI are inaccessible

Examples:

• Patients with spinal cord or head injury often cannot be moved to the CT scanner
• Continuous monitoring
• Ambulances or remote locations
• During pulmonary procedures

Some Medical Applications of EIT

- Monitoring ventilation and perfusion in ARDS patients
- Diagnosis of atelectasis, pnuemothorax, lung collapse and hyperdistension, and pleural effusion
- Visualization and quantitative measures from pulmonary function tests (PFT's)
- Identifying regions of obstruction or consolidation in children with cystic fibrosis (CF)

Some Medical Applications of EIT

- Monitoring ventilation and perfusion in ARDS patients
- Diagnosis of atelectasis, pnuemothorax, lung collapse and hyperdistension, and pleural effusion
- Visualization and quantitative measures from pulmonary function tests (PFT's)
- Identifying regions of obstruction or consolidation in children with cystic fibrosis (CF)

In the ICU:
• Patients with spinal cord or head injury often cannot be moved to the CT scanner
• Small pneumothoraces and atelectasis are not visible with portable x-rays

Governing Equations

Let $\gamma(x) = \sigma(x) + i\omega\epsilon(x)$. Then

$$\nabla \cdot (\gamma(x)\nabla u(x)) = 0, \quad x \in \Omega$$

Knowledge of all voltage patterns on the boundary arising from all possible current density patterns on the boundary:

$$R_\gamma : \gamma \frac{\partial u}{\partial \nu}|_{\partial\Omega} \to u|_{\partial\Omega}$$ Neumann-to-Dirichlet map

$$\Lambda_\gamma : u|_{\partial\Omega} \to \gamma \frac{\partial u}{\partial \nu}|_{\partial\Omega}$$ Dirichlet-to-Neumann map

Ill-posedness

EIT is an ill-posed problem since the solution does not depend continuously on the data Λ_σ.
This means given any $\epsilon > 0$ and any $\delta > 0$, there exist conductivity distributions $\sigma_1(z)$ and $\sigma_2(z)$ such that

$$\|\Lambda_{\sigma_1} - \Lambda_{\sigma_2}\|_{H^{1/2}(\partial\Omega)\to H^{-1/2}(\partial\Omega)} < \delta$$

but

$$\|\sigma_1 - \sigma_2\|_{L^\infty(\Omega)} > \epsilon.$$

This is evident in

- The classic example by Alessandrini
- Analysis of simulated or experimental data

Alessandrini's example

Consider the two conductivity distributions on the unit disk Ω

$$\sigma_1(r,\theta) = 1, \qquad \sigma_2(r,\theta) = \begin{cases} 1+A, & 0 \le r \le R \\ 1, & R < r \le 1 \end{cases}$$

satisfying

$$\begin{array}{cc} \nabla \cdot (\sigma_1 \nabla u_1) = 0, \quad \text{in} \quad \Omega & \nabla \cdot (\sigma_2 \nabla u_2) = 0, \quad \text{in} \quad \Omega \\ u_1|_{\delta\Omega} = \phi & u_2|_{\delta\Omega} = \phi \end{array}$$

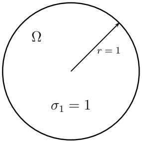

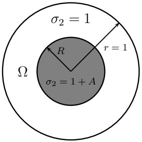

Alessandrini's example

The solution of the forward problem can be found by separation of variables and the current on the boundary can be computed (by hand).

As a result, the difference of the DN maps applied to ϕ is

$$(\Lambda_{\sigma_1} - \Lambda_{\sigma_2})\phi = \sum_{n=-\infty}^{\infty} |n| \left(\frac{-2AR^{2|n|}}{2 + A(1 - R^{2|n|})} \right) \phi_n e^{in\theta}$$

Alessandrini's example

Since

$$\left| \frac{-2AR^{2|n|}}{2 + A(1 - R^{2|n|})} \right| \leq AR,$$

we have the bound

$$\|\Lambda_{\sigma_1} - \Lambda_{\sigma_2}\|_{H^{1/2}(\partial\Omega) \to H^{-1/2}(\partial\Omega)} \leq AR,$$

which can be made arbitrarily small, depending on the choice of R. However, independent of R,

$$\|\sigma_1 - \sigma_2\|_{L^\infty(\Omega)} = A,$$

which can be chosen greater than ϵ.

An example from simulated data

Consider two phantoms: One representing healthy lungs and the other with a pneumothorax (ptx) in one lung:

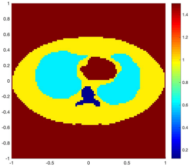

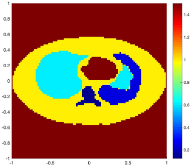

At right are the first three voltages arising from trignometric CPs on 32 electrodes with 1 mA current amplitude

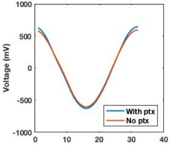

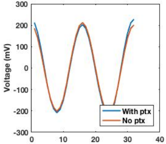

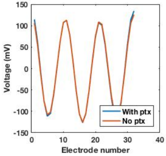

An example from simulated data

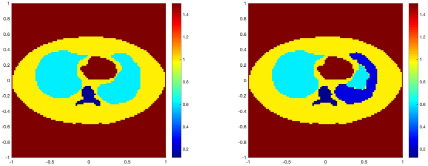

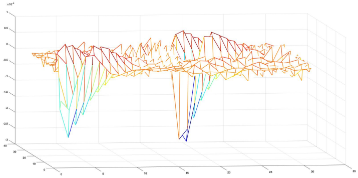

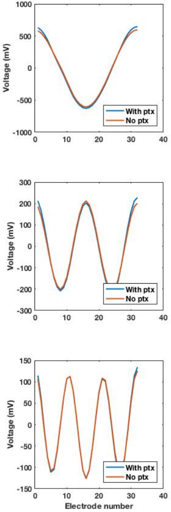

This is the difference in the DN maps for the two cases (z axis scale is 10^{-4})

Further difficulties

In addition to the inherent ill-posedness of the problem:

- Measurements are finite precision and contain noise
- There is uncertainty/error in the electrode placement
- The domain shape may be imperfectly known/changing
- The skin-electrode effect (contact impedance) must be modeled

These provide challenges and opportunities for mathematicians!

Reconstruction Algorithms

Existing Reconstruction Algorithms fall into several categories:

- Least-squares algorithms
- Statistical inversion
- Linearization algorithms
- D-bar methods

State of the art typically includes modeling of errors, inclusion of priors, and attention to real-time capabilities

Least-squares Algorithms

Iteratively solve

$$\min_{\sigma_i} \|\mathbf{V} - \mathbf{U}\|_2^2 + \alpha\|\vec{\sigma} - \vec{\sigma}_{pr}\|_2^2$$

The forward problem must be solved at each iteration

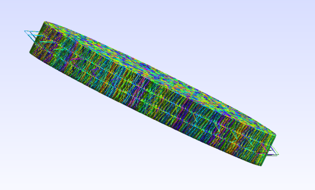

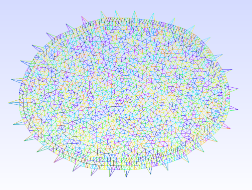

Describe the conductivity as a vector of piecewise constant values over the N mesh elements

$$\sigma(x) \approx \sum_{n=1}^{N} \sigma_n \chi(E_n)$$

State of the art: The size of the FEM mesh can be reduced by applying the approximation error theory [Kaipio and Somersalo, 2004], using Bayesian modeling to treat approximation and modeling errors.

Least-squares Algorithms

Using the generalized Tikhonov regularization theory

$$F(\rho) = \frac{1}{2}(\phi_m^q - \phi_e^q(\rho))^T(\phi_m^q - \phi_e^q(\rho)) \; + \lambda^2(\rho - \rho^*)^T L^T L(\rho - \rho^*)$$

Statistical priors such as an anatomical atlas can be used in the regularization, replacing it by

$$\gamma^2(\rho - \bar{\rho}_{sw})^T \; \Gamma_{sw}^{-1} \; (\rho - \bar{\rho}_{sw}) + \lambda^2(\rho - \bar{\rho}_{sw})^T \; F^T F \; (\rho - \bar{\rho}_{sw})$$

$\bar{\rho}_{sw}$ is the expected values vector, Γ_{sw} is the covariance matrix of the anatomical atlas. Assume the probability density function of the resistivity distribution in the swine thorax, $\pi(\rho_{sw})$, can be described as a Gaussian distribution:

$$\pi(\rho_{sw}) \propto e^{-\frac{1}{2}(\rho - \bar{\rho}_{sw})^T \; \Gamma_{sw}^{-1} \; (\rho - \bar{\rho}_{sw})} \tag{1}$$

Least-squares Algorithms

This was demonstrated in [Camargo, 2013] using a set of 39 CT scans of pig chests from 25 animals. For each CT scan, 5 images at different levels were used (center, $\pm$20mm and $\pm$40mm), generating a 3-dimensional image. Five different tissues – bones, aerated lungs, atelectasis, heart and muscles – were identified according to their characteristics concerning grey levels.

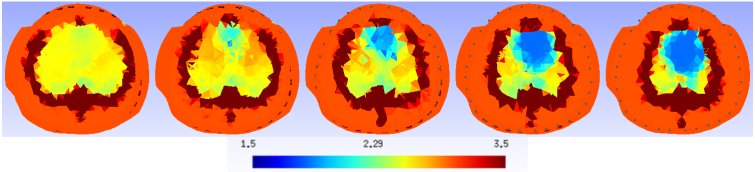

A Gaussian distribution of resistivity was assigned to each segmented tissue of the tomographic images.

Source: Erick D.L.B. Camargo, In: A review of electrical impedance tomography in lung applications: Theory and algorithms for absolute images, Martins et al, Annual Reviews in Control, 2019

Gauss-Newton

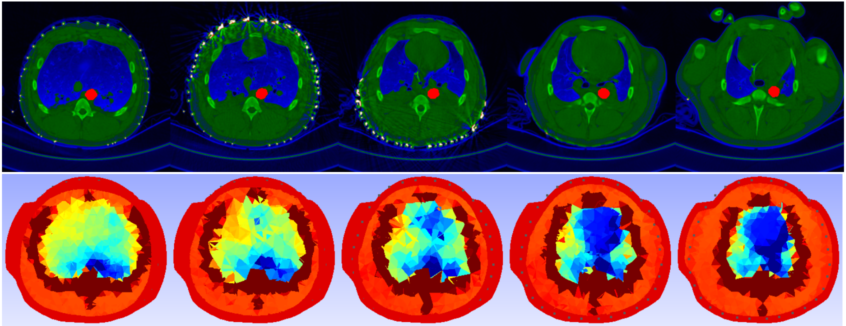

Top: Five CT scan slices of a pig ventilated with PEEP of $5cmH_2O$. The aorta is marked in light red. Bottom: EIT resistivity images computed with the G-N method using an anatomical atlas. (Scale $1.5 \leq \rho \leq 3.5\Omega - m$)

Source: Erick D.L.B. Camargo, In: A review of electrical impedance tomography in lung applications: Theory and algorithms for absolute images, Martins et al, Annual Reviews in Control, 2019

Kalman filter

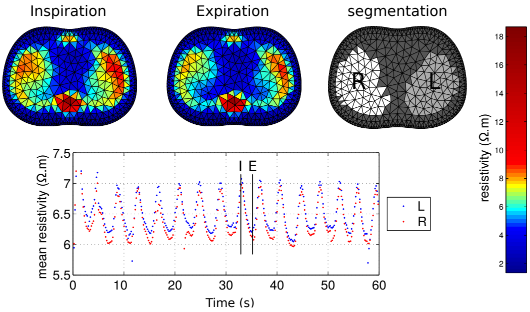

Human in vivo resistivity estimation using dual estimation with the unscented Kalman filter in parallel with the parameters in a two compartment evolution model of lung mechanics. Top: representative images from inspiration (I) and expiration (E). Bottom: average resistivity in each lung as a function of time.

Source: Fernando Moura, In: A review of electrical impedance tomography in lung applications: Theory and algorithms for absolute images, Martins et al, Annual Reviews in Control, 2019

Calderón’s method

Calderón’s method solves the linearized problem by direct inversion:

$$\begin{aligned}\hat{\gamma}(k) &= -\frac{1}{2|k|^2}\int_{\partial\Omega} e^{\pi i(k\cdot x)+\pi(a\cdot x)}\Lambda_\gamma(e^{\pi i(k\cdot x)-\pi(a\cdot x)})ds + R(k)\\ &= \hat{F}(k) + R(k),\, a, z \in \mathbb{R}^n \;\text{ with }\; |a| = |z| \;\text{ and }\; a\cdot z = 0.\end{aligned}$$

Truncation of the integral in the inverse Fourier transform regularizes the solution

R=0.0075

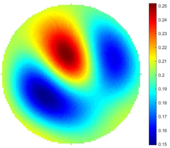

R=0.009

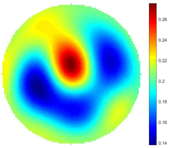

Images computed by Kwancheol Shin, CSU

Calderón’s method

Calderón’s method with a second order correction term and priors improves spatial resolution

$$\hat{\gamma}(k) = \begin{cases} \hat{F}(k), & |k| \leq R_1 \\ \hat{\gamma}_{pr}(k), & R_1 < |k| \leq R_2 \\ 0, & |k| > R_2 \end{cases},$$

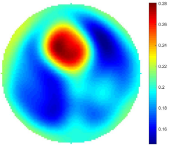

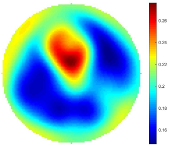

R=0.0075 R=0.009

Images computed by Kwancheol Shin, CSU

General Overview: D-bar Methods for EIT

$\star$ D-bar reconstruction methods capitalize on the direct relationship between the conductivity and CGO solutions to a PDE related to the inverse conductivity problem

$$\Lambda_\sigma \longrightarrow \psi(z,k) \longrightarrow \mathbf{t}(k) \longrightarrow \mu(z,k) \longrightarrow \sigma(z)$$

They are

- Nonlinear
- Mesh independent
- Trivially parallelizable

Equations of the D-bar Method based on [N, 1996]

$$\Lambda_\sigma \longrightarrow \psi(z,k) \longrightarrow \mathbf{t}(k) \longrightarrow \mu(z,k) \longrightarrow \sigma(z)$$

Equations of the D-bar Method based on [N, 1996]

Change of variables:

$$q(z) = \Delta\sqrt{\sigma(z)}/\sqrt{\sigma(z)}, \quad \psi(z) = \sqrt{\sigma(z)}u(z)$$

$$\Lambda_\sigma \longrightarrow \psi(z,k) \longrightarrow \mathbf{t}(k) \longrightarrow \mu(z,k) \longrightarrow \sigma(z)$$

Equations of the D-bar Method based on [N, 1996]

Change of variables:

$$q(z) = \Delta\sqrt{\sigma(z)}/\sqrt{\sigma(z)}, \quad \psi(z) = \sqrt{\sigma(z)}u(z)$$

Schrödinger Eqn: $(-\Delta + q)\psi = 0 \quad \text{in } \mathbb{R}^2$

$$\Lambda_\sigma \longrightarrow \psi(z,k) \longrightarrow \mathbf{t}(k) \longrightarrow \mu(z,k) \longrightarrow \sigma(z)$$

Equations of the D-bar Method based on [N, 1996]

Change of variables:

$$q(z) = \Delta\sqrt{\sigma(z)}/\sqrt{\sigma(z)}, \quad \psi(z) = \sqrt{\sigma(z)}u(z)$$

Schrödinger Eqn: $(-\Delta + q)\psi = 0 \quad \text{in } \mathbb{R}^2$

Lippmann-Schwinger Eqn: $\mu = 1 - g_k * q\mu$ where

$$\mu = e^{-ikz}\psi$$

and g_k is fund. soln. for $-\Delta - 4ik\bar{\partial}$

$$\Lambda_\sigma \longrightarrow \psi(z,k) \longrightarrow \mathbf{t}(k) \longrightarrow \mu(z,k) \longrightarrow \sigma(z)$$

Equations of the D-bar Method based on [N, 1996]

Change of variables:
$$q(z) = \Delta\sqrt{\sigma(z)}/\sqrt{\sigma(z)}, \quad \psi(z) = \sqrt{\sigma(z)}u(z)$$

Schrödinger Eqn: $(-\Delta + q)\psi = 0 \quad$ in $\mathbb{R}^2$

Lippmann-Schwinger Eqn: $\mu = 1 - g_k * q\mu$ where
$$\mu = e^{-ikz}\psi$$
and g_k is fund. soln. for $-\Delta - 4ik\bar{\partial}$

$$\Lambda_\sigma \longrightarrow \psi(z,k) \longrightarrow \mathbf{t}(k) \longrightarrow \mu(z,k) \longrightarrow \sigma(z)$$

$$\psi(z,k)|_{\partial\Omega} = e^{ikz}|_{\partial\Omega} - \int_{\partial\Omega} G_k(z-\zeta)(\Lambda_\sigma - \Lambda_1)\psi(\cdot,k)ds(\zeta)$$
where $G_k = e^{ikz}g_k$

Equations of the D-bar Method based on [N, 1996]

$$\mathbf{t}(k) = \int_{\mathbb{R}^2} e^{i\bar{k}\bar{z}} q(z)\psi(z,k)dz$$

Nonlinear Fourier transform of q

$$\Lambda_\sigma \longrightarrow \psi(z,k) \longrightarrow \mathbf{t}(k) \longrightarrow \mu(z,k) \longrightarrow \sigma(z)$$

Equations of the D-bar Method based on [N, 1996]

$$\mathbf{t}(k) = \int_{\mathbb{R}^2} e^{i\bar{k}\bar{z}} q(z)\psi(z,k)dz$$

Nonlinear Fourier transform of q

$$\Lambda_\sigma \longrightarrow \psi(z,k) \longrightarrow \mathbf{t}(k) \longrightarrow \mu(z,k) \longrightarrow \sigma(z)$$

$$\mathbf{t}(k) = \int_{\partial\Omega} e^{i\bar{k}\bar{z}} (\Lambda_\sigma - \Lambda_1)\psi(z,k)ds(z)$$

Relates Λ_σ to ψ

Equations of the D-bar Method based on [N, 1996]

$$\boxed{\bar{\partial}_k \mu(z,k) = \frac{\mathbf{t}(k)}{4\pi\bar{k}} e^{-i(zk+\bar{z}\bar{k})}\overline{\mu(z,k)}}$$

$$\Lambda_\sigma \longrightarrow \psi(z,k) \longrightarrow \mathbf{t}(k) \longrightarrow \mu(z,k) \longrightarrow \sigma(z)$$

Equations of the D-bar Method based on [N, 1996]

$$\bar{\partial}_k \mu(z,k) = \frac{\mathbf{t}(k)}{4\pi\bar{k}} e^{-i(zk+\bar{z}\bar{k})} \overline{\mu(z,k)}$$

$$\Lambda_\sigma \longrightarrow \psi(z,k) \longrightarrow \mathbf{t}(k) \longrightarrow \mu(z,k) \longrightarrow \sigma(z)$$

$$\mu(z,k) = 1 + \frac{1}{(2\pi)^2} \int_{\mathbb{R}^2} \frac{\mathbf{t}(k')}{(k-k')\bar{k'}} e^{-i(zk'+\bar{z}\bar{k'})} \overline{\mu(z,k')} dk'$$

Equations of the D-bar Method based on [N, 1996]

$$\boxed{\sigma(z) = \mu^2(z,0)}$$

$$\Lambda_\sigma \longrightarrow \psi(z,k) \longrightarrow \mathbf{t}(k) \longrightarrow \mu(z,k) \longrightarrow \sigma(z)$$

Scattering transform encodes data non-intuitively

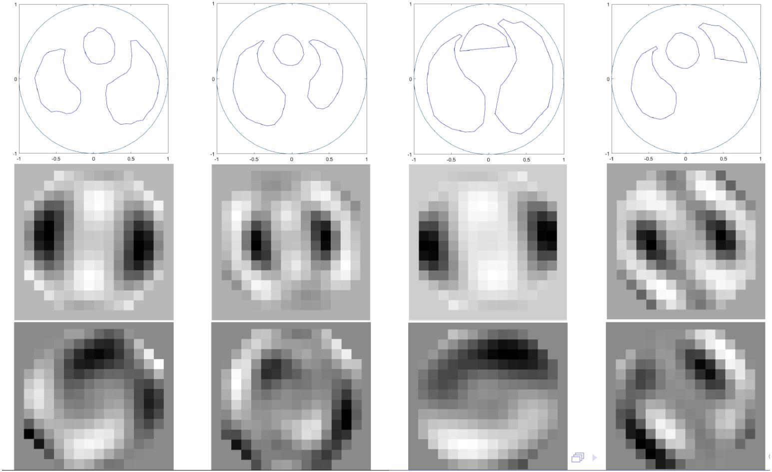

Source: Michael Capps, PhD thesis, Colorado State University, 2019

Convolutional neural network

Question: Could machine learning be used in the characterization of the scattering transform to identify where the boundaries are?

Convolutional neural network

Question: Could machine learning be used in the characterization of the scattering transform to identify where the boundaries are?

A convolutional neural network was trained on 200,000 scattering transforms computed from numerically simulated data sets.

Two “base” sets of internal boundaries were used:

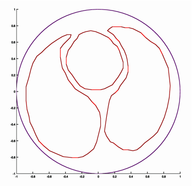

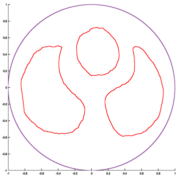

Convolutional neural network

Question: Could machine learning be used in the characterization of the scattering transform to identify where the boundaries are?

A convolutional neural network was trained on 200,000 scattering transforms computed from numerically simulated data sets.

Two “base” sets of internal boundaries were used:

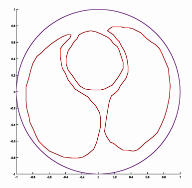

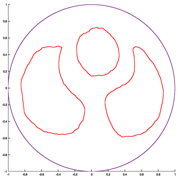

Network input: Two-channel greyscale images: one channel for $\Re(\mathbf{t}(k))$ and one channel for $\Im(\mathbf{t}(k))$.

Network output: a vector of points in $\mathbb{R}^2$ corresponding to points on the boundaries of internal structures.

Training data

The following parameters in each numerically simulated data set were randomized:

- Boundary scale (55%-105%)
- Conductivities of each organ ($\pm$ 50% from base conductivities of 2 S/m and 0.5 S/m for the heart and lungs)
- Truncation radius ($4 \leq R \leq 8$)
- Simulated organ injuries (25% chance of having the bottom 20%-70% of the organ removed)
- Mollification factor

$\mathbf{t}(k)$ was evaluated on a 16×16 grid and the internal boundaries were sampled at 52 points.

Results on simulated data

The network was applied to 50 examples of scattering transforms not used in training, some corresponding to multiple lung injuries:

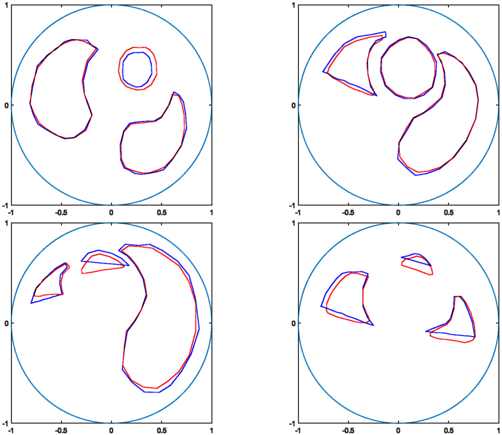

Blue: true boundaries, Red: Network predicted boundaries

Source: Michael Capps, PhD thesis, Colorado State University, 2019

Results on tank data

Agar “heart” 238 mS/m and agar “lungs” 136 mS/m were placed in saline 190 mS/m in a 32 electrode tank
Data was collected at 125 kHz with current amplitude 3.3 mA

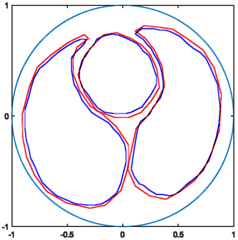

Blue: true boundaries, Red: Network predicted boundaries

Source: Michael Capps, PhD thesis, Colorado State University, 2019

Cystic Fibrosis

CF is a genetic disease characterized by lung congestion and infection and malabsorption of nutrients by the pancreas

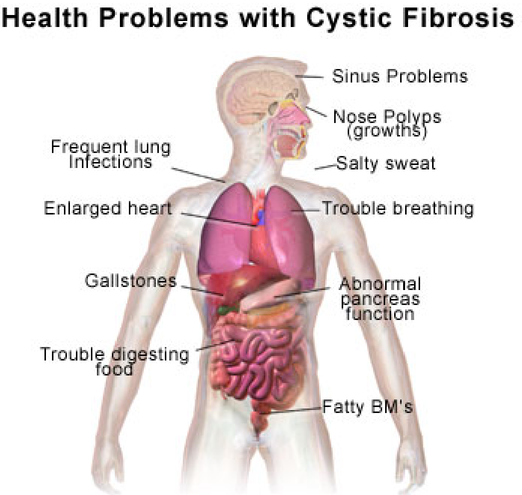

Cystic Fibrosis

The lungs exhibit air trapping and consolidation due to mucus plugging and airway thickening

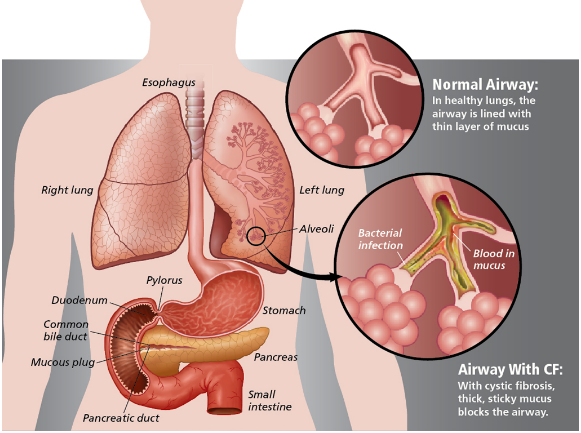

An *A Priori* D-bar Algorithm

Define a piecewise scattering transform to use in place of the usual $\mathbf{t}(k)$:

$$\mathbf{t}_{R_1,R_2}(k) := \begin{cases} \mathbf{t}(k), & |k| \leq R_1 \\ \mathbf{t}_{\mathrm{pr}}(k), & R_1 < |k| \leq R_2 \\ 0, & |k| > R_2 \end{cases},$$

To compute $\mathbf{t}_{\mathrm{pr}}$, we use the definition:

$$\mathbf{t}_{\mathrm{pr}}(k) = \int_{\mathbb{R}^2} e^{i\bar{k}\bar{z}} q_{\mathrm{pr}}(z)\psi_{\mathrm{pr}}(z,k)dz,$$

This avoids having to numerically simulate data using FEM.

Solve the constrained nonlinear optimization problem

$$\underset{\mathbf{c}\in\mathbb{R}^n}{\text{minimize}} \;\; F(\mathbf{c}) := \|\mathbf{t}_{\mathrm{pr}}^{\mathrm{vec}}(\mathbf{c}) - \mathbf{t}^{\mathrm{vec}}\|_2^2, \;\; \text{subject to} \;\; \ell_i \leq c_i \leq u_i, \; 1 \leq i \leq n$$

D-bar method with a prior

Three time snapshots during exhalation of a CF subject:

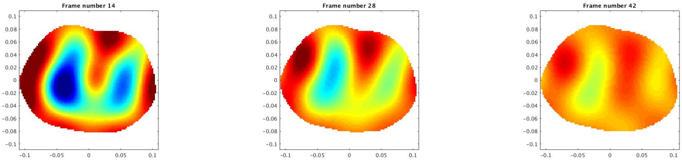

Peak inhalation | partial exhalation | further exhalation

D-bar method with a prior

Three time snapshots during exhalation of a CF subject:

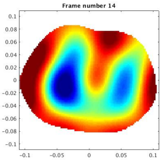

Peak inhalation

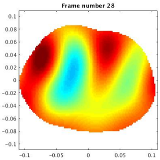

partial exhalation

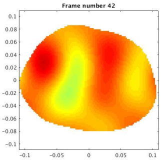

further exhalation

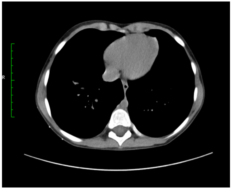

Inspiratory CT scan

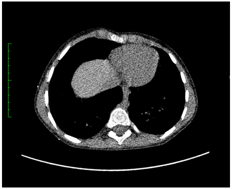

Expiratory CT scan

Alsaker, M., Murthy, J. of Comp. and Appl. Math. **362**, 2019

D-bar method with a prior

The dynamic prior:

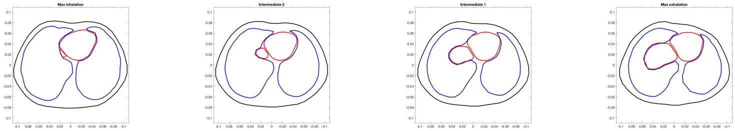

D-bar method with a prior

The dynamic prior:

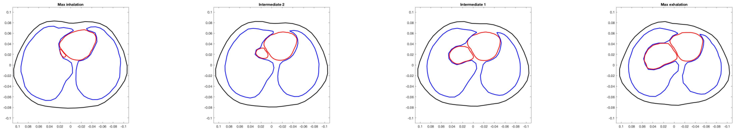

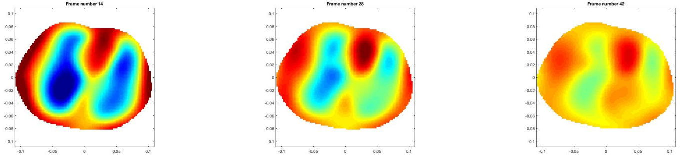

Peak inhalation partial exhalation further exhalation

Alsaker, M., Murthy, J. of Comp. and Appl. Math. **362**, 2019

Air-trapping findings

- EIT-derived ventilation-perfusion $\dot{V}/\dot{Q}$ index maps were computed from three subjects at Children's Hospital Colorado
- Subjects A and B were cystic fibrosis patients with significant air trapping (AT) in their lungs. Subject B exhibited the most AT. The radiologist reported "extensive regions of air trapping, regional to the lung areas affected by the bronchial and alveolar plugging which appears to be approximately 50% of both lungs."
- Dark blue regions in the EIT $\dot{V}/\dot{Q}$ index maps represent regions well-perfused but poorly ventilated (AT)
- Global and regional $\dot{V}/\dot{Q}$ indices are computed by summing over the ROI

Subject	$\dot{V}/\dot{Q}$ global	$\dot{V}/\dot{Q}$ left lung	$\dot{V}/\dot{Q}$ right lung
Healthy Control	0.4625	0.4870	0.4172
CF Subject A	0.3377	0.1999	0.4209
CF Subject B	0.1024	0.0665	0.1148

DICOM orientation (left lung on viewer's right)

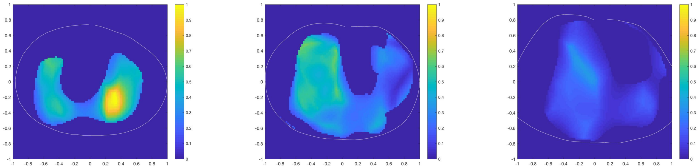

EIT $\dot{V}/\dot{Q}$ index maps from healthy control (left), CF subject A (center), and CF subject B (right)

M., Muller, Mellenthin, Murthy, Capps, Alsaker, Deterding, Sagel, DeBoer, Phys. Meas., **39** 2018

Conclusions

What does the future of EIT hold?

- Need to address challenges such as partial boundary data
- 3-D algorithms are needed for accurate volume computations
- Clinical studies must be performed with the best hardware and software
- Priors will surely be part of clinical algorithms
- It will be filling the niches that CT and MRI cannot fill

Thank you!!